Polymer Bulletin (2021) 78:2389–2404
https://doi.org/10.1007/s00289-020-03216-1

ORIGINAL PAPER

Effect of α-Fe_2O_3 nanoparticles on the mechanism of charge storage in polypyrrole-based hydrogel

Vitaly K. Vorobiov[1] · **Alexander N. Bugrov**[1,2] · **Igor A. Kasatkin**[3] ·
Sergey A. Bolshakov[2] · **Maria P. Sokolova**[1] · **Nikolay N. Smirnov**[1] ·
Michael A. Smirnov[1]

Received: 8 November 2019 / Revised: 12 March 2020 / Accepted: 23 April 2020 / Published online: 3 May 2020

Abstract

A hybrid hydrogel based on polypyrrole and hydrothermally prepared α-Fe_2O_3 nanoparticles was synthesized via in situ chemical polymerization of pyrrole using sodium trimetaphosphate as a crosslinker. Wide-angle X-ray diffraction study confirmed the presence of α-Fe_2O_3 in the prepared material. Mapping of the elemental composition using energy dispersive X-ray spectroscopy showed the uniform distribution of the inorganic particles inside the polypyrrole matrix. The effect of α-Fe_2O_3 on the structure of the hybrid hydrogel and on the mechanism of charge storage was studied with scanning electron microscopy, cyclic voltammetry, galvanostatic charge–discharge and impedance spectroscopy. The specific capacitance was found to increase from 250 F g^{-1} for the polypyrrole hydrogel up to 509 F g^{-1} for the α-Fe_2O_3-doped hydrogel at the current density of 0.2 A g^{-1}. The hematite incorporation also affected the morphology of the hydrogel leading to a slight increase in the double-layer capacitance accompanied with a strong increase in the pseudocapacitance: from 239 F g^{-1} up to 486 F g^{-1}. The initial polypyrrole hydrogel and the hybrid hydrogel demonstrated a capacitance retention of about 75% and 79% after 3000 charge–discharge cycles at the current density of 4 A g^{-1}, respectively.

Keywords Hydrogel · Hydrothermal synthesis · Polypyrrole · Hematite · Supercapacitor · Nanoparticles

---

Electronic supplementary material The online version of this article (https://doi.org/10.1007/s00289-020-03216-1) contains supplementary material, which is available to authorized users.

✉ Vitaly K. Vorobiov
vrbvrbvrb@mail.ru

[1] Institute of Macromolecular Compounds, Russian Academy of Sciences, Saint Petersburg, Russia

[2] Department of Physical Chemistry, Saint Petersburg Electrotechnical University “LETI”, Saint Petersburg, Russia

[3] Saint Petersburg State University, Saint Petersburg, Russia

Introduction

As a power source, supercapacitors (SCs) fill the niche between the conventional electrochemical batteries and the dielectric capacitors. They demonstrate a higher cycle stability and power density than the former [1, 2] and a higher energy density than the latter. To achieve the beneficial characteristics of SCs, elaboration of porous electroconducting and ionically conducting materials containing electrochemically active additives or chemical groups is required. This will allow for effective utilization of double-layer capacitance and fast faradaic redox reactions (pseudocapacitance) [3].

Recently, electrode materials for SCs based on electrically conductive polymers (ECPs)—polypyrrole (PPy), polyaniline, polythiophene and their derivatives have attracted a considerable interest due to their advantages such as electrical conductivity, flexibility, redox activity and easy control of morphology during synthesis [4]. When used as electrode materials, electroactive polymer hydrogels (EPHs) demonstrate electrical and ionic conductivity simultaneously inside the whole volume of an electrode. Porous electroactive hydrogels facilitate ion transport in the material that increases the power density of the electrode [5, 6].

The specific capacitance can be improved by introduction of electrochemically active additives which increase the pseudocapacitance of the material. For this purpose, the composites of ECPs with organic [7–9] and inorganic additives are intensively studied. The most commonly used inorganic additives are the electroactive transition metal oxides (EOs), such as MnO_2 [10, 11], Fe_2O_3 [12, 13], and CeO_2 [14, 15], which are not hazardous and have a high theoretical specific capacitance.

The α-Fe_2O_3 (hematite) nanoparticles with the n-type semiconductor properties are among the most promising EOs used in the preparation of the supercapacitor electrodes [16, 17]. They are electrochemically stabile [18] and have a suitable band gap (2.0–2.2 eV) [19], high values of specific power (2250 W kg^{-1}) and energy (63.15 W kg^{-1}) [20]; they also have a large specific capacitance: the maximum reported value achieved for α-Fe_2O_3 nanostructures was 340.5 F g^{-1} [21]. As a rule, smaller hematite particles with a large surface-to-volume ratio allow to achieve a higher capacitance [22]. Hydrothermal synthesis is the most versatile method used for the preparation of fine nanoparticles: the morphology and crystallite size of the product can be controlled by tuning the temperature, pressure, isothermal holding time and the composition of the hydrothermal environment [23]. Additionally, hematite nanoparticles incorporated into the PPy matrix increase the electrical conductivity of the PPy due to a more dense packing of macromolecules on the polymer-particle interface [24]. It is worthy to mention that suchlike hybrid hydrogels demonstrate a combined pseudocapacitance due to simultaneous reversible redox transitions of PPy chains and iron atoms.

Insufficient electrical contact between ECPs and EOs and inhomogeneous distribution of the particles in the polymer matrix deteriorate the beneficial properties of the hybrid materials. This can be partially avoided by synthesis of ECPs in the form of a thin layer on the EOs [25–27] or by synthesis of EOs directly on the surface (or in the bulk) of ECPs [28, 29]. At the same time, a porous, swellable form of ECPs—the EPHs—increases the availability of EOs for insertion/extraction of the electrolyte counter-ions inside the composite electrode, which is a prerequisite for pseudocapacitance.

The EPHs have a continuous electroconducting network with a high ion penetration rate in the polymer bulk [30]. Various EPHs have been synthesized by crosslinking the polymer chains via the hydrogen bonds or ionic interactions: using phytic acid [31, 32], trypan blue [33], or amino trimethylene phosphoric acid [34]. EPHs have also been produced by polymerization of pyrrole or aniline within another hydrogel based, for instance, on polyvinyl alcohol (PVA) [35, 36], acrylic acid-g-cellulose nanocrystals [37], poly(acrylic acid) [38], heparin-methacrylate [39], 3,4-poly(ethylenedioxythiophene) and poly(sodium 4-styrenesulfonate) [40], or by formation of a branched polymer structure (polyaniline-graft-polyacrylamide) [30].

Sodium trimetaphosphate (STMP) is a low cost and eco-friendly non-toxic and water-soluble salt that has been widely utilized in biomedical applications and in food industry as a crosslinker for such polysaccharides as starch [41], dextran [42], pullulan [43], xanthan gum [44] and synthetic polymers such as PVA [45, 46], PVA/poly(*N*-vinyl-2-pyrrolidone) [47]. STMP can be easily prepared by annealing NaH_2PO_4.

The purpose of this work was to synthesize a hybrid hydrogel based on polypyrrole and α-Fe_2O_3 nanoparticles, to investigate the effect of the nanoparticles on the structure of the material and on the mechanism of charge storage.

Experimental

Materials

Acrylamide (AAm), pyrrole (99%, extra pure), *N*,*N*,*N*′,*N*′-tetramethylethylenediamine (TEMED) were purchased from Sigma-Aldrich, methanol (> 99.5%)—from (Vekton, Russia), ammonium persulfate (APS) (99%), $Fe(NO_3)_3 \times 9H_2O$ and NH_4OH (≥ 25% NH_3 in H_2O) were purchased from Neva Reactive (Russia). All of the materials were used as received without purification. STMP was prepared from $NaH_2PO_4 \times H_2O$ (Vekton, Russia) by annealing at 400 °C for 8 h, and its chemical structure was confirmed with wide angle X-ray diffraction. Polyacrylamide (PAAm) was prepared and characterized according to our previous work [30]. Pyrrole (Sigma-Aldrich) was distilled under vacuum prior to use.

Synthesis of iron oxide nanoparticles

$Fe(NO_3)_3 \times 9H_2O$ (4.04 g) was dissolved in 20 ml of distilled water. The ammonia solution in water (25 wt%) was added dropwise until pH = 9 was reached. The resulting brown precipitate of iron hydroxide was repeatedly washed with distilled water until a negative reaction to NO_3^- ions was observed, and then dried in air at 60 °C until reaching constant weight. Subsequently, the X-ray amorphous powder of $Fe(OH)_3$ was dehydrated under hydrothermal conditions at 120 °C and 7 MPa for 10 h. The resulting suspension of hematite nanoparticles was removed from the autoclave and dried at 60 °C on air until the constant mass was reached.

Synthesis of PPy-STMP hydrogel

The synthesis of PPy-STMP hydrogels was carried out on carbon tissue inside a spacer with inner diameter 1.2 cm and height 2 mm. In a typical synthesis, 2.6 mg of pyrrole was dissolved in 77 μl of water–methanol mixture 5:2 (by volume) containing 0.78 mg PAAm and 2 mg of STMP. The reaction mixture was sonicated for 5 min at 25 °C and then put onto the carbon tissue. After that 8.8 mg of ammonium persulfate dissolved in 55 μl of a water–methanol mixture 1:2 (by volume) was quickly added to the reaction mixture. The obtained solution was kept overnight. In the text below this sample is marked as PPy-STMP.

Synthesis of PPy-STMP-Fe_2O_3hybrid hydrogel

The PPy-STMP hydrogel with the iron oxide particles imbedded in it was prepared by the same method as the PPy-STMP hydrogel with an addition of the powdered α-Fe_2O_3 (0.6 mg). The inorganic particles were added to the solution of pyrrole, STMP and PAAm. The amount of pyrrole was reduced in order to maintain approximately the same total mass of the active material on the electrode as was taken for PPy-STMP without metal oxide: $m(PPy+Fe_2O_3)=2.6$ mg. Prior to polymerization, the dispersion was sonicated for 2 h at 25 °C in order to achieve a uniform distribution of the particles in the final material. Further in the text the hybrid hydrogel sample is marked as PPy-STMP-Fe_2O_3. A photograph of the as-prepared PPy-STMP and PPy-STMP-Fe_2O_3 hydrogel samples are given in ESI (Fig. S1a and b, respectively).

Characterization of hydrogels

Scanning and transmission electron microscopy

The morphology of both hydrogels was studied by scanning electron microscopy (SEM) using of Tescan scanning electron microscope VEGA 3 SBH (Czech Republic). Distribution of the α-Fe_2O_3 nanoparticles and of the crosslinking agent (STMP) in the hybrid material was characterized by energy dispersive X-ray (EDX) spectroscopy using an Aztec Energy X-act microanalysis system (Oxford Instruments, UK).

The shape and size of the α-Fe_2O_3 nanoparticles formed under hydrothermal conditions were determined by transmission electron microscopy (TEM) using a transmission electron microscope Jeol JEM-2100F (Japan) operated at the accelerating voltage of 200 kV with the point resolution of 0.19 nm. The TEM samples were prepared by casting drops of the hematite aqueous dispersions on a copper grid covered with ultrathin graphene paper.

X-ray diffraction study

The prepared hydrogels were investigated with wide-angle X-ray diffraction (WAXD) using a D2 PHASER diffractometer (Bruker, Germany) equipped with a CuK$_\alpha$ radiation source ($\lambda = 1.54056$ Å) within the 2θ range of 15°– 65° with the scan step of 0.05°.

Fourier-transform infrared spectroscopy investigation

Fourier-transform infrared (FTIR) spectra were taken with an IRAffinity-1S spectrometer (Shimadzu, Japan) within the range of 1800–500 cm^{-1} for the dried and powdered hydrogels using KBr pellets in the transmission mode with the resolution of 1 cm^{-1} and 100 scans per sample.

Electrochemical measurements

Electrochemical measurements of the hydrogel samples were performed in a three-electrode set-up with the hydrogel working electrode (mass of the active material was 2.6 mg) prepared in situ on the carbon cloth. Ag/AgCl was used as a reference and the Pt coil as a counter electrode. The 1 mol l^{-1} water solution of Na_2SO_4 was used as the electrolyte.

Cyclic voltammetry (CV), galvanostatic charge–discharge (GCD) and electrochemical impedance measurements were performed with a P40-X potentiostat–galvanostat equipped with a module for impedance measurements FRA-24 (Elins, Russia). Specific capacitance of the material (C) was calculated from the discharge branches of the GCD curves as $C = It/(m(\Delta U - U_{\mathrm{IR}}))$, where I is the electrical current, t is the time to full discharge, ΔU is the potential window, U_{IR} is the IR drop, and m is the mass of the active material on the working electrode. The methodology suggested by Trasatti et al. [48] was used to distinguish between the double-layer capacitance and the pseudocapacitance arising due to electrochemical redox reactions inside the volume of the electrode material. For this purpose, the CV curves of the investigated samples were measured at the scan rates of 0.5–20 mV s^{-1} and the specific capacitance (C_{CV}) at each scan rate was calculated according to equation:

$$C_{\mathrm{CV}} = \frac{1}{2vm\left(U_2 - U_1\right)} \int_{U_1}^{U_2} i(U)\mathrm{d}U,$$

where v is the scan rate, $i(U)$ is the current dependence on the potential, U_1 and U_2 are the lowest and the highest potentials within the scanning range, respectively.

Electrochemical impedance study was performed under the open circuit potential in the frequency range of 400 kHz–10 mHz. The experimental data was fitted using the equation for impedance of an equivalent circuit:

$$Z = R_{\mathrm{s}} + \frac{1}{1/\left(Z_{\mathrm{w}} + R_{\mathrm{ct}}\right) + 1/Z_{\mathrm{CPE}}},$$

where Z_w and Z_{CPE} are the impedances of the Warburg and CPE elements, respectively, described by the following equations:

$$Z_W = \frac{A}{(j\omega)^{1/2}} \coth\left(B(j\omega)^{\frac{1}{2}}\right) \text{ and } Z_{CPE} = \frac{1}{Q(j\omega)^{\alpha}},$$

where ω and j are the angular frequency and the imaginary unit, while α, Q, A and B are the refinable parameters.

Results and discussion

Hydrothermal synthesis of α-Fe_2O_3 nanoparticles

Hematite nanoparticles prepared under hydrothermal conditions from inorganic precursors (chlorides, nitrates or sulfates) [14, 49–52] could have spherical, hexagonal, pseudo-cubic, rod-like or anisometric morphology with average sizes in the range of 30–100 nm depending on the temperature and duration of the treatment. In this work, the conditions were adjusted to obtain α-Fe_2O_3 nanoparticles with an average size of less than 10 nm to ensure a high surface area. For this purpose, the dehydration was conducted at a relatively low temperature (120 °C) during 10 h. Prior to hydrothermal synthesis, $Fe(OH)_3$ was carefully washed to remove salt-forming ions. This lowered the mass transfer rate and hampered the recrystallization processes that led to the formation of small crystallites. TEM results shown in Fig. 1 demonstrate the mean size of the prepared hematite nanoparticles of 5 ± 2 nm. At the same time, larger rhombohedral crystallites with their sizes of 20–30 nm could also be found. Their appearance could probably be related to partial coalescence of the smaller

Fig. 1 TEM micrograph of α-Fe_2O_3 nanoparticles

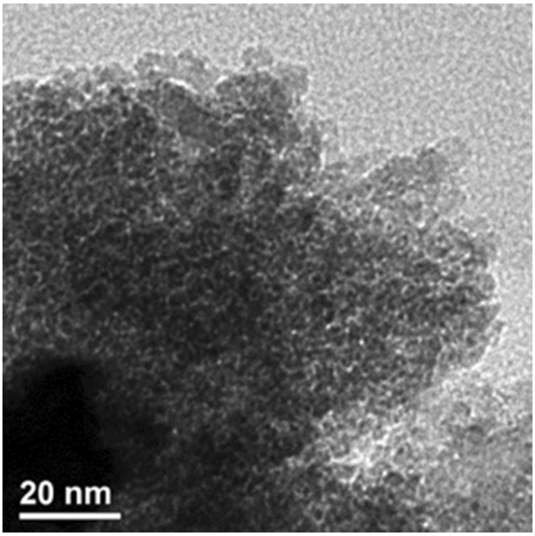

hematite nanoparticles. Nevertheless, the oxide particles used in this work were, on average, smaller than in the other works reported in the literature.

Chemical structure and morphology of hydrogels

The electroactive hydrogels based on PPy crosslinked with STMP and the hybrid hydrogels containing iron oxide nanoparticles were prepared by in situ oxidative polymerization of pyrrole monomer with peroxydisulfate ammonia. The chemical structure of the prepared materials was examined with FTIR spectroscopy. The corresponding spectra are shown in Fig. 2. The characteristic PPy [53] (930, 966, 1049, 1200, 1288, 1478, 1554 cm^{-1}) and PAAm [54] (1103, 1450, 1679 cm^{-1}) bands are clearly observed in the spectra. The band at 1707 cm^{-1} can be attributed to C=O stretching vibrations of the overoxidized or hydrolyzed pyrrole group. The weak shoulder near 1326 cm^{-1} can be attributed to the vibration of the P–O bonds that indicates the appearance of STMP molecules in the structure of the hydrogel. Two strong absorption bands in the region of 400–600 cm^{-1}, which are characteristic of α-Fe_2O_3 [55, 56], are not visible in the spectrum of the hybrid hydrogel. This can be explained by a dense and highly IR-absorbing [57] PPy layer covering the oxide nanoparticles. However, this required that the successful incorporation of Fe_2O_3 in the prepared hydrogel should be verified with other methods.

The results of WAXD measurements for prepared Fe_2O_3 nanoparticles shown in Fig. 3 confirm their hematite structure (ICDD PDF #29–0713) [58]. The diffraction pattern of the PPy-STMP hydrogel demonstrates only an amorphous hallo with a

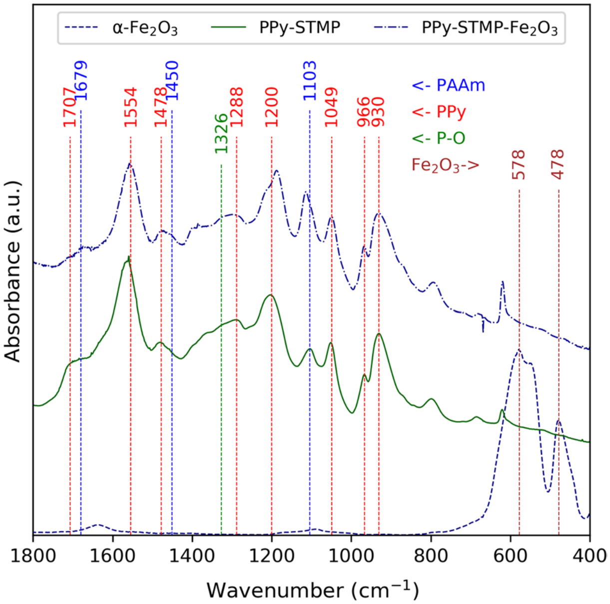

Fig. 2 FTIR spectra of the α-Fe_2O_3, PPy-STMP and PPy-STMP-Fe_2O_3 samples

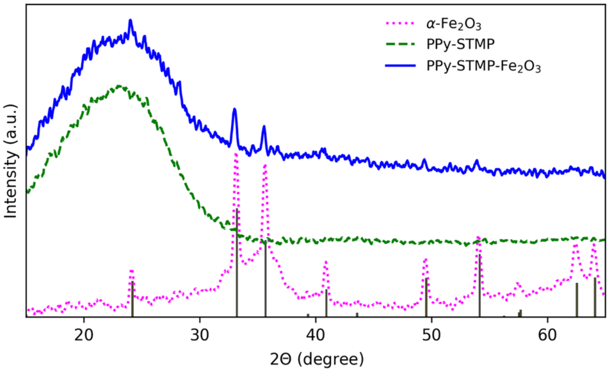

Fig. 3 X-ray diffraction patterns of dry samples. Vertical lines demonstrate positions of the α-Fe_2O_3 reflections according to ICDD PDF #29–0713

maximum at about 2θ = 22° typical of PPy prepared with an addition of polyacrylamide [59]. Absence of sharp peaks confirms the successful incorporation of STMP as a counter ion inside the PPy hydrogel. PPy-STMP hydrogel synthesized in the presence of hematite nanoparticles displays reflections typical of α-Fe_2O_3.

SEM images of the initial and hybrid hydrogels (Fig. 4a, b, respectively) demonstrate agglomerated granular morphology typical of the PPy-based materials.

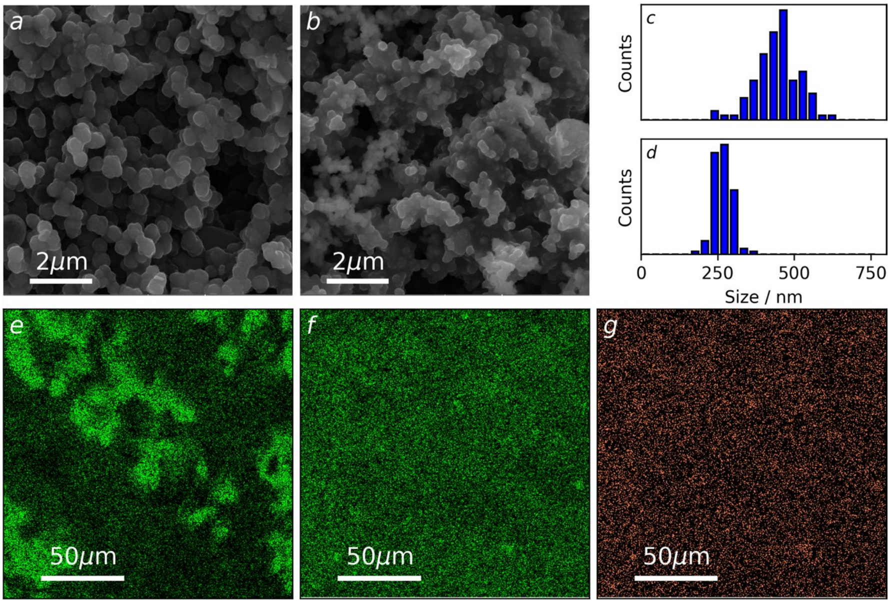

Fig. 4 SEM images of PPy-STMP (**a**), PPy-STMP-Fe_2O_3 (**b**), size distribution of PPy granules in PPy-STMP (**c**) and PPy-STMP-Fe_2O_3 (**d**) and EDX elemental mapping of P for PPy-STMP (**e**), P (**f**) and Fe (**g**) for PPy-STMP-Fe_2O_3

Introduction of the oxide particles in the hydrogel matrix leads to a denser packed morphology with smaller granules (Fig. 4b). The densification takes place due to, probably, specific interactions between the iron oxide nanoparticles and PPy via hydrogen bonding. Agglomeration of the hematite nanoparticles is not observed in the hybrid hydrogels that suggest their uniform distribution in the material. The average size of the PPy particles seen in the SEM images (Fig. 4c, d) decreases from 450 nm in PPy-STMP to 250 nm in PPy-STMP-Fe_2O_3. Fe^{3+} ions can act as an additional oxidizer for the pyrrole monomer, thus increasing the nucleation rate and the resulting polymerization rate during formation of PPy.

The EDX maps of phosphorus distribution for the PPy-STMP and PPy-STMP-Fe_2O_3 samples are shown in Fig. 4e and f, respectively. It is seen that the distribution of the crosslinker is not uniform in the initial hydrogel. This can reflect the process of microsyneresis inside the PPy-STMP hydrogel that can be responsible for the formation of the porous structure visible in Fig. 4a. The distribution of the crosslinker in the hybrid hydrogel is much more uniform (Fig. 4f), although some fluctuations of the P concentration can still be seen. Figure 4g illustrates a homogeneous distribution of Fe in the PPy-STMP-Fe_2O_3 hybrid material. This gives an additional evidence of the high compatibility between the electroconducting PPy matrix and the oxide nanoparticles in the hybrid gel, that is beneficial for the electrochemical properties. This is in agreement with the results of mechanical measurements in compression mode, which are given in ESI (see Table S1 and Fig. S2). This is seen that the hybrid hydrogel is noticeably more durable and rigid than the pure PPy hydrogel. This is possibly related to additional crosslinking of the polypyrrole by iron oxide nanoparticles.

Electrochemical properties of PPy-STMP hydrogels

The electrochemical capacitance of the PPy and hybrid hydrogels was studied using the GCD technique in a three-electrode cell in the potential range between − 0.5 and 0.5 V vs Ag/AgCl reference. The discharge branches of the curves demonstrate a difference in the electrochemical behavior between the organic and hybrid hydrogels (Fig. 5a, b, respectively). The curve for the PPy-STMP-Fe_2O_3 hydrogel demonstrates a step in the potential range − 0.1… − 0.3 V vs Ag/AgCl which is not observed in the PPy-STMP hydrogel. The appearance of the step can be connected with a partial reduction of the iron ions (Fe^{3+}/Fe^{2+}) on the surface of the nanoparticles. This pseudocapacitive process increases the specific capacitance of the hybrid hydrogel at low current density (0.2 A g^{-1}) up to the value of 509 F g^{-1} in comparison with the pure organic hydrogel that demonstrates only 250 F g^{-1}.

The maximum specific capacitance found in our samples (509 F g^{-1} at 0.2 A g^{-1}) is close to the maximal values reported for other similar materials based on PPy and iron oxides. For example, only 106 F g^{-1} at 0.4 mA g^{-1} were reported for PPy/γ-Fe_2O_3 samples prepared via electrochemical synthesis of PPy in the presence of Fe_2O_3 nanoparticles [60]; 140 F g^{-1} at 0.2 A g^{-1} was measured for a ternary composite containing PPy, α-Fe_2O_3 and graphene oxide, prepared via two-step preparation method including hydrothermal synthesis of Fe_2O_3 nanoparticles with

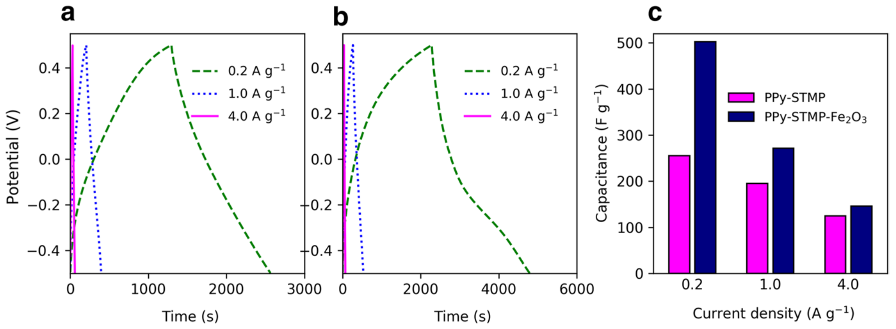

Fig. 5 Galvanostatic charge–discharge curves for PPy-STMP (**a**) and PPy-STMP-Fe_2O_3 (**b**) samples at different current densities and specific capacitances for the prepared hydrogels (**c**)

subsequent in situ oxidative polymerization of pyrrole [61]; 311 F g^{-1} at 2 A g^{-1} for a sample based on the PPy with a mixture of iron oxides (FeO, Fe_2O_3 and Fe_3O_4) and Na-carboxymethylcellulose, obtained via galvanostatic electrodeposition from a solution containing pyrrole, $Fe(BF_4)_2$ and Na-carboxymethylcellulose [62]. Nevertheless, the PPy@Fe_2O_3 samples prepared at 180 °C via one-step hydrothermal method starting from $Fe(NO_3)_3$ and pyrrole demonstrated 560 F g^{-1} at 5 A g^{-1} [63].

As seen in Fig. 5c, the difference between the samples is significantly reduced with increasing current density. At the current density of 4 A g^{-1} the capacitance of PPy-STMP-Fe_2O_3 is only 25% higher than that of the pure PPy-STMP sample: 150 and 120 F g^{-1}, respectively, due to, probably, a limited speed of the faradaic process in the PPy-STMP-Fe_2O_3 sample. To separate the contributions of pseudocapacitance (C_p) and double-layer capacitance (C_{dl}) to the total capacitance (C_{total}), the samples were studied using CV with subsequent data analysis according to the Trasatti method [48, 59–61]. For this purpose, the CV experiments were conducted at the scan rates from 0.5 (Fig. 6a) up to 20 mV s^{-1} (Fig. 6b). The results are presented in Fig. 6c in the form of the capacitance dependencies on the reciprocal square root of the scan rate ($C(v^{-1/2})$), and in Fig. 6d as the dependencies of the reciprocal capacitance on the square root of the scan rate ($C^{-1}(v^{1/2})$). According to the Trasatti method, the linear extrapolation of $C(v^{-1/2})$ dependence to $x=0$ (i.e. to infinitely high v) gives the value of the "scan rate independent" capacitance of the "outer" surface, which is considered as the double-layer capacitance (C_{dl}). The total capacitance (C_{total}) that includes both the "inner" surface capacitance and C_{dl} can be found by linear extrapolation of $C^{-1}(v^{1/2})$ dependence to $x=0$ (i.e. infinitely low v). The "inner" surface capacitance connected with the ion insertion process can be considered as a pseudocapacitance (C_p) because the insertion/release of anions into/from the hybrid hydrogel is accompanied with an oxidation/reduction processes of the PPy chains and/or by Fe^{2+}/Fe^{3+} transition. Thus, the value of C_p can be calculated as $C_p = C_{total}–C_{dl}$. The values of C_{dl} found by extrapolation were 99 and 111 F g^{-1}, while the total capacitance values were 338 and 597 F g^{-1} for PPy-STMP and PPy-STMP-Fe_2O_3, respectively. A small increase in C_{dl} of the hybrid hydrogel in comparison with the pure PPy-STMP

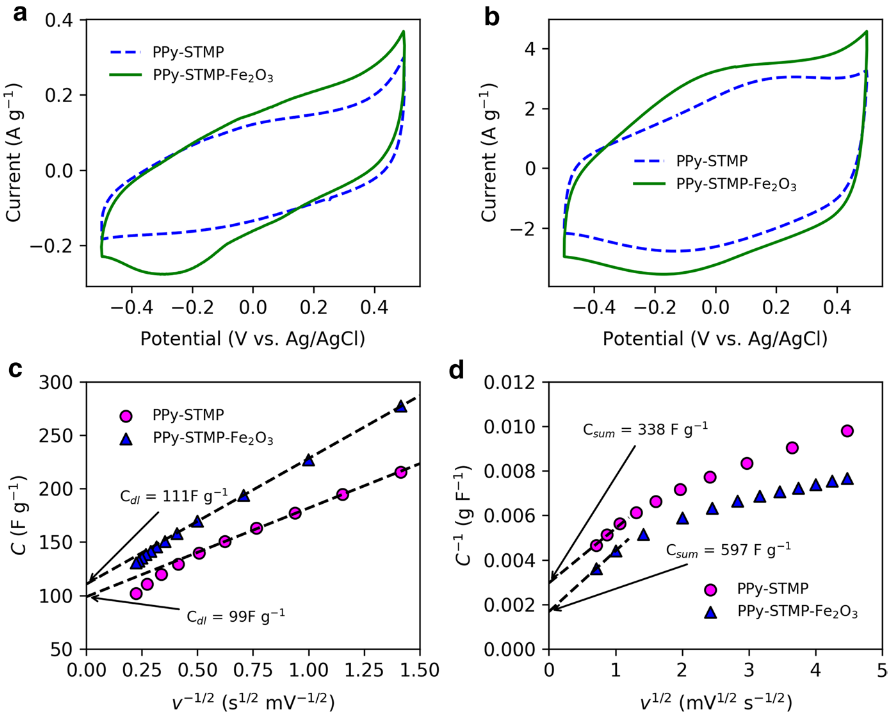

Fig. 6 Cyclic voltammograms of the PPy-STMP and PPy-STMP-Fe_2O_3 samples at the scan rates of 0.5 (**a**) and 20 mV s^{-1} (**b**); the capacitance dependence on the square root of the reciprocal scan rate (**c**), and the reciprocal capacitance dependence on the square root of scan rate (**d**)

hydrogel can be connected with a decrease in the average size of the PPy granules due to introduction of the α-Fe_2O_3 nanoparticles. At the same time, the values of C_p were 239 F g^{-1} and 486 F g^{-1} for PPy-STMP and PPy-STMP-Fe_2O_3, respectively. It could be proposed, that the additional capacitance of 247 F g^{-1} was provided by the Fe_2O_3 nanoparticles. If the 23% mass fraction of the oxide on the electrode was taken into account, the resulting (recalculated) value of 1070 F g^{-1} (relatively to the mass of Fe_2O_3 only, i.e. 0.6 mg) would be comparable with the best results reported in the literature for Fe_2O_3 [21]. Thus, the oxide incorporated into an electrode based on the conducting polymer hydrogel gets effectively involved into the electrochemical charge storage process.

The electrochemical impedance study was conducted within the frequency region of 400 kHz—10 mHz under the open circuit potential in the three electrode cells. The impedance spectra and their fitting according to equivalent circuit (Fig. 7c) are shown in Fig. 7a and b for PPy-STMP and PPy-STMP-Fe_2O_3, respectively. The parameters of the equivalent circuit, found by fitting, are given in Table 1.

As seen in Fig. 7, the experimental points are well fitted with the equivalent circuit. Table 1 shows that the parameters of the Warburg element and R_{ct} are

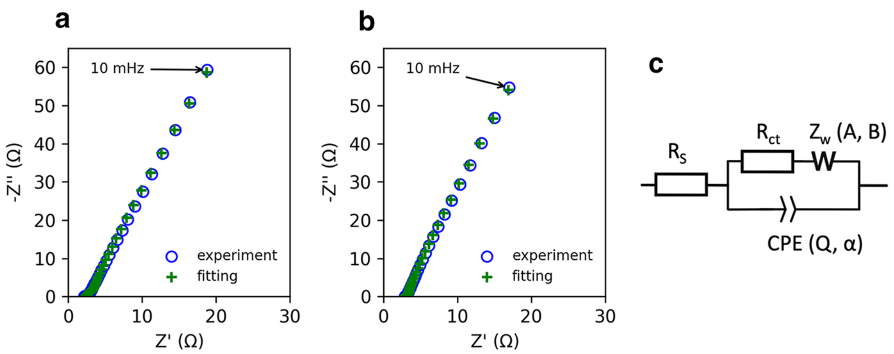

Fig. 7 Electrochemical impedance spectra of PPy-STMP (**a**), PPy-STMP-Fe_2O_3 (**b**) and the equivalent circuit used for fitting the experimental data (**c**)

Table 1 The refined parameters of the equivalent circuit

Sample	A	B	Q	α	R_{ct}	R_s
PPy-STMP	11.8	0.8	0.10	0.77	0.70	2.3
PPy-STMP-Fe_2O_3	5.5	0.5	0.10	0.76	0.05	2.8

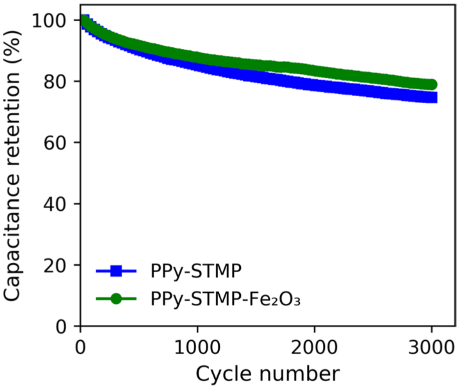

Fig. 8 Electrochemical cycling stability of the PPy-STMP and PPy-STMP-Fe_2O_3 hydrogels at the current density of 4 A g^{-1}

significantly higher for the PPy-STMP-Fe_2O_3 sample. The parameter A of Z_w is connected with the diffusion and concentration of the redox-active components, and R_{ct} reflects the rate of the redox process. The lower values of these parameters for the hybrid hydrogel suggest a stronger effect of the redox process in the whole electrochemical performance of the doped material in comparison with the pure PPy-STMP hydrogel. Thus, doping with the oxide particles increased the pseudocapacitance of the material. This result is in agreement with other electrochemical measurements.

The samples were tested for cycling stability by applying 3000 charge–discharge cycles at the current density of 4 A g^{-1}. The calculated dependences of the capacitance retention on the number of cycles are shown in Fig. 8. It can be seen that the PPy-STMP and PPy-STMP-Fe_2O_3 hydrogels have similar values of the retention ratio of 75 and 79%, respectively. These are moderate values: for example, a α-Fe_2O_3 nanorods/polyaniline/carbon nanotubes hydrogel reported in [64] demonstrated 96.3% capacitance retention after 10,000 cycles at the scan rate of 100 mV s^{-1}, while a graphene/Fe_2O_3 composite hydrogel maintained 75% of the initial capacitance after 200 cycles at the scan rate of 20 mV s^{-1} [65]. The degradation observed during cycling was probably caused by a mechanical destruction (swelling-shrinking) of the material during the charge–discharge process. A better cycle stability of the composite hydrogel could result from the Fe_2O_3 nanoparticles acting as additional crosslinking centers.

Conclusions

The pure PPy-STMP and PPy-STMP-Fe_2O_3 hybrid hydrogels were synthesized by in situ chemical polymerization. The hybrid hydrogel demonstrated a specific capacitance of 509 F g^{-1} that is more than two times higher than the value for the pure PPy hydrogel (250 F g^{-1}) at the current density of 0.2 A g^{-1}. The α-Fe_2O_3 nanoparticles prepared hydrothermally and uniformly distributed in the PPy matrix contributed to a stronger effect of pseudocapacitance. In addition, the capacitance retention during cycling of the hybrid hydrogel is not lower than of the initial PPy-STMP hydrogel: 79% of the initial capacitance retained after 3000 cycles at the current density of 4 A g^{-1}. The average size and the distribution width of the PPy granules decreased dramatically (from 450 to 250 nm) upon addition of the Fe_2O_3 nanoparticles. This structural change leads to a 10% increase in double layer capacitance.

Acknowledgments The reported study was funded by Russian Foundation for Basic Research (Grant 18-03-01167 a). The experimental work was facilitated by the equipment of the Research Centre for X-ray Diffraction Studies at St. Petersburg State University and of the Engineering Center of the St. Petersburg State Technological Institute (Technical University). The authors are grateful to Dr. I.S. Kuryndin for mechanical measurements.

References

1. Wang G, Zhang L, Zhang J (2012) A review of electrode materials for electrochemical supercapacitors. Chem Soc Rev 41:797–828. https://doi.org/10.1039/c1cs15060j
2. Pérez-Madrigal MM, Estrany F, Armelin E et al (2016) Towards sustainable solid-state supercapacitors: electroactive conducting polymers combined with biohydrogels. J Mater Chem A 4:1792–1805. https://doi.org/10.1039/c5ta08680a
3. Dubal DP, Chodankar NR, Kim DH, Gomez-Romero P (2018) Towards flexible solid-state supercapacitors for smart and wearable electronics. Chem Soc Rev 47:2065–2129. https://doi.org/10.1039/c7cs00505a
4. Meng Q, Cai K, Chen Y, Chen L (2017) Research progress on conducting polymer based supercapacitor electrode materials. Nano Energy 36:268–285. https://doi.org/10.1016/j.nanoen.2017.04.040
5. Smirnov MA, Sokolova MP, Geydt P et al (2017) Dual doped electroactive hydrogelic fibrous mat with high areal capacitance. Mater Lett 199:192–195. https://doi.org/10.1016/j.matlet.2017.04.083
6. Armelin E, Pérez-Madrigal MM, Alemán C, Díaz DD (2016) Current status and challenges of biohydrogels for applications as supercapacitors and secondary batteries. J Mater Chem A 4:8952–8968. https://doi.org/10.1039/c6ta01846g

7. Patil DS, Pawar SA, Devan RS et al (2013) Electrochemical supercapacitor electrode material based on polyacrylic acid/polypyrrole/silver composite. Electrochim Acta 105:569–577. https://doi.org/10.1016/j.electacta.2013.05.022
8. Davoglio RA, Biaggio SR, Bocchi N, Rocha-Filho RC (2013) Flexible and high surface area composites of carbon fiber, polypyrrole, and poly(DMcT) for supercapacitor electrodes. Electrochim Acta 93:93–100. https://doi.org/10.1016/j.electacta.2013.01.062
9. Wang Z, Tammela P, Huo J et al (2016) Solution-processed poly (3,4-ethylenedioxythiophene) nanocomposite paper electrodes for high-capacitance flexible supercapacitors. J Mater Chem A 4:1714–1722. https://doi.org/10.1039/C5TA10122K
10. Wang JG, Yang Y, Huang ZH, Kang F (2014) MnO2/polypyrrole nanotubular composites: reactive template synthesis, characterization and application as superior electrode materials for high-performance supercapacitors. Electrochim Acta 130:642–649. https://doi.org/10.1016/j.electacta.2014.03.082
11. Lu Q, Zhou Y (2011) Synthesis of mesoporous polythiophene/MnO2 nanocomposite and its enhanced pseudocapacitive properties. J Power Sources 196:4088–4094. https://doi.org/10.1016/j.jpowsour.2010.12.059
12. Ren S, Ma S, Yang Y et al (2015) Hydrothermal synthesis of Fe2O3/polypyrrole/graphene oxide composites as highly efficient electrocatalysts for oxygen reduction reaction in alkaline electrolyt. Electrochim Acta 178:179–189. https://doi.org/10.1016/j.electacta.2015.07.181
13. Arjomandi J, Lee JY, Movafagh R et al (2018) Polyaniline/aluminum and iron oxide nanocomposites supercapacitor electrodes with high specific capacitance and surface area. J Electroanal Chem 810:100–108. https://doi.org/10.1016/j.jelechem.2017.12.086
14. Xie A, Tao F, Li T et al (2018) Graphene-cerium oxide/porous polyaniline composite as a novel electrode material for supercapacitor. Electrochim Acta 261:314–322. https://doi.org/10.1016/j.electacta.2017.12.165
15. Kumar AM, Babu RS, Ramakrishna S, de Barros ALF (2017) Electrochemical synthesis and surface protection of polypyrrole-CeO2 nanocomposite coatings on AA2024 alloy. Synth Met 234:18–28. https://doi.org/10.1016/j.synthmet.2017.10.003
16. Hjiri M, Aida MS, Neri G (2019) NO2 selective sensor based on α-Fe2O3 nanoparticles synthesized via hydrothermal technique. Sensors 19:1–11. https://doi.org/10.3390/s19010167
17. Chaudhari NK, Chaudhari S, Yu JS (2014) Cube-like α-Fe2O3 supported on ordered multimodal porous carbon as high performance electrode material for supercapacitors. Chemsuschem 7:3102–3111. https://doi.org/10.1002/cssc.201402526
18. Shivakumara S, Penki TR (2014) Preparation and electrochemical performance of porous hematite (α-Fe2O3) nanostructures as supercapacitor electrode material. J Solid State Electrochem 18:1057–1066. https://doi.org/10.1007/s10008-013-2355-1
19. Kamali KZ, Alagarsamy P, Huang NM et al (2014) Hematite nanoparticles-modified electrode based electrochemical sensing platform for dopamine. Sci World J 2014:1–13. https://doi.org/10.1155/2014/396135
20. Li B, Sun Q, Fan H et al (2018) Morphology-controlled synthesis of hematite nanocrystals and their optical, magnetic and electrochemical performance. Nanomaterials 8:1–12. https://doi.org/10.3390/nano8010041
21. Zhu M, Wang Y, Meng D et al (2012) Hydrothermal synthesis of hematite nanoparticles and their electrochemical properties. J Phys Chem C 116:16276–16285. https://doi.org/10.1021/jp304041m
22. Zhang X, Niu Y, Li Y et al (2013) Synthesis, optical and magnetic properties of α-Fe2O3 nanoparticles with various shapes. Mater Lett 99:111–114. https://doi.org/10.1016/j.matlet.2013.02.070
23. Lin M, Tng L, Lim T et al (2014) Hydrothermal synthesis of octadecahedral hematite (α-Fe2O3) nanoparticles: an epitaxial growth from goethite (α-FeOOH). J Phys Chem C 118:10903–10910. https://doi.org/10.1021/jp502087h
24. Gangopadhyay R, De A (2000) Conducting polymer nanocomposites: a brief overview. Chem Mater 12:608–622. https://doi.org/10.1021/cm990537f
25. Fu S, Ma L, Gan M et al (2017) 3D reduced graphene oxide/MnO2/polyaniline composite for high-performance supercapacitor. J Mater Sci Mater Electron 28:3621–3629. https://doi.org/10.1007/s10854-016-5964-5
26. Mu B, Zhang W, Shao S, Wang A (2014) Glycol assisted synthesis of graphene-MnO2-polyaniline ternary composites for high performance supercapacitor electrodes. Phys Chem Chem Phys 16:7872–7880. https://doi.org/10.1039/c4cp00280f

27. Benhaddad L, Bernard MC, Deslouis C et al (2013) Chemical synthesis of hollow sea urchin like nanostructured polypyrrole particles through a core-shell redox mechanism using a MnO2 powder as oxidizing agent and sacrificial nanostructured template. Synth Met 175:192–199. https://doi.org/10.1016/j.synthmet.2013.05.010
28. He Y, Du S, Li H et al (2016) MnO2/polyaniline hybrid nanostructures on carbon cloth for supercapacitor electrodes. J Solid State Electrochem 20:1459–1467. https://doi.org/10.1007/s10008-016-3162-2
29. Wang H, Wang X, Peng C et al (2015) Preparation and the electrochemical performance of MnO2/PANI@CNT composite for supercapacitors. J Nanosci Nanotechnol 15:709–714. https://doi.org/10.1166/jnn.2015.9166
30. Smirnov MA, Sokolova MP, Bobrova NV et al (2016) Capacitance properties and structure of electroconducting hydrogels based on copoly(aniline - P-phenylenediamine) and polyacrylamide. J Power Sources 304:102–110. https://doi.org/10.1016/j.jpowsour.2015.11.035
31. Wang Z, Tammela P, Zhang P et al (2014) Freestanding nanocellulose-composite fibre reinforced 3D polypyrrole electrodes for energy storage applications. Nanoscale 6:13068–13075. https://doi.org/10.1039/c4nr04642k
32. Xu D, Xiao X, Cai J et al (2015) Highly rate and cycling stable electrode materials constructed from polyaniline/cellulose nanoporous microspheres. J Mater Chem A 3:16424–16429. https://doi.org/10.1039/c5ta03917g
33. Yang C, Zhang P, Nautiyal A et al (2019) Tunable three-dimensional nanostructured conductive polymer hydrogels for energy-storage applications. ACS Appl Mater Interfaces 11:4258–4267. https://doi.org/10.1021/acsami.8b19180
34. Heydari H, Gholivand MB (2016) An all-solid-state asymmetric device based on a polyaniline hydrogel for a high energy flexible supercapacitor. New J Chem 41:237–244. https://doi.org/10.1039/C6NJ02266A
35. Ding Q, Xu X, Yue Y et al (2018) Nanocellulose-Mediated Electroconductive self-healing hydrogels with high strength, plasticity, viscoelasticity, stretchability, and biocompatibility toward multifunctional applications. ACS Appl Mater Interfaces 10:27987–28002. https://doi.org/10.1021/acsami.8b09656
36. Zang L, Liu Q, Qiu J et al (2017) Design and fabrication of an all-solid-state polymer supercapacitor with highly mechanical flexibility based on polypyrrole hydrogel. ACS Appl Mater Interfaces 9:33941–33947. https://doi.org/10.1021/acsami.7b10321
37. Li Y, Zhang H, Ni S, Xiao H (2018) In situ synthesis of conductive nanocrystal cellulose/polypyrrole composite hydrogel based on semi-interpenetrating network. Mater Lett 232:175–178. https://doi.org/10.1016/j.matlet.2018.08.115
38. Smirnov MA, Bobrova NV, Dmitriev IY et al (2011) Electroactive hydrogels based on poly(acrylic acid) and polypyrrole. Polym Sci - Ser A 53:67–74. https://doi.org/10.1134/S0965545X11010068
39. Access O, Ding H, Zhong M et al (2014) Biologically derived soft conducting hydrogels using heparin-doped polymer networks. ACS Nano 8:4348–4357. https://doi.org/10.1021/nn406019m
40. Dai T, Tang R, Yue X et al (2015) Capacitance performances of supramolecular hydrogels based on conducting polymers. Chinese J Polym Sci (English Ed) 33:1018–1027. https://doi.org/10.1007/s10118-015-1647-6
41. Wang S, Chen X, Shi M et al (2015) Absorption of whey protein isolated (WPI)-stabilized β-Carotene emulsions by oppositely charged oxidized starch microgels. Food Res Int 67:315–322. https://doi.org/10.1016/j.foodres.2014.11.041
42. Riahi N, Liberelle B, Henry O, De Crescenzo G (2017) Impact of RGD amount in dextran-based hydrogels for cell delivery. Carbohydr Polym 161:219–227. https://doi.org/10.1016/j.carbpol.2017.01.002
43. Autissier A, Le Visage C, Pouzet C et al (2010) Fabrication of porous polysaccharide-based scaffolds using a combined freeze-drying/cross-linking process. Acta Biomater 6:3640–3648. https://doi.org/10.1016/j.actbio.2010.03.004
44. Tao Y, Zhang R, Xu W et al (2016) Rheological behavior and microstructure of release-controlled hydrogels based on xanthan gum crosslinked with sodium trimetaphosphate. Food Hydrocoll 52:923–933. https://doi.org/10.1016/j.foodhyd.2015.09.006
45. Chaouat M, Le Visage C, Baille WE et al (2008) A novel cross-linked poly(vinyl alcohol) (PVA) for vascular grafts. Adv Funct Mater 18:2855–2861. https://doi.org/10.1002/adfm.200701261

46. Leone G, Bidini A, Lamponi S, Magnani A (2013) States of water, surface and rheological characterisation of a new biohydrogel as articular cartilage substitute. Polym Adv Technol 24:824–833. https://doi.org/10.1002/pat.3150
47. Leone G, Consumi M, Greco G et al (2011) A PVA/PVP hydrogel for human lens substitution: synthesis, rheological characterization, and in vitro biocompatibility. J Biomed Mater Res Part B Appl Biomater 97:278–288. https://doi.org/10.1002/jbm.b.31813
48. Ardizzone S, Fregonara G, Trasatti S (1990) "Inner" and "outer" active surface of RuO2 electrodes. Electrochim Acta 35:263–267. https://doi.org/10.1016/0013-4686(90)85068-X
49. Ma J, Lian J, Duan X et al (2010) α-Fe2O3: Hydrothermal synthesis, magnetic and electrochemical properties. J Phys Chem C 114:10671–10676. https://doi.org/10.1021/jp102243g
50. Qin W, Yang C, Yi R, Gao G (2011) Hydrothermal synthesis and characterization of single-crystalline α-Fe2O3 nanocubes. J Nanomater 2011:3–8. https://doi.org/10.1155/2011/159259
51. Wang F, Qin XF, Meng YF et al (2013) Hydrothermal synthesis and characterization of α-Fe2O 3 nanoparticles. Mater Sci Semicond Process 16:802–806. https://doi.org/10.1016/j.mssp.2012.12.029
52. Chaudhari S, Bhattacharjya D, Yu JS (2013) 1-Dimensional porous α-Fe2O3 nanorods as high performance electrode material for supercapacitors. RSC Adv 3:25120–25128. https://doi.org/10.1039/c3ra44159h
53. Omastová M, Trchová M, Kovářová J, Stejskal J (2003) Synthesis and structural study of polypyrroles prepared in the presence of surfactants. Synth Met 138:447–455. https://doi.org/10.1016/S0379-6779(02)00498-8
54. Murugan R, Mohan S, Bigotto A (1998) FTIR and polarized Raman spectra of acrylamide and polyacrylamide. J Kor Phys Soc 32:505–512
55. Wang Y, Muramatsu A, Sugimoto T (1998) FTIR analysis of well-defined alpha-Fe2O3 particles. Colloids Surfaces A Physicochem Eng Asp 134:281–297. https://doi.org/10.1016/S0927-7757(97)00102-7
56. Farahmandjou M, Soflaee F (2015) Synthesis and characterization of α-Fe_2O_3 nanoparticles by simple co-precipitation method. Phys Chem Res 3:191–196. https://doi.org/10.22036/pcr.2015.9193
57. Andreeva OA, Burkova LA, Smirnov MA, El'Yashevich GK (2006) Correlation between IR spectra and electric conductivity of polyethylene-polypyrrole composites. Polym Sci Ser B 48:331–334. https://doi.org/10.1134/S1560090406110066
58. Morris MC, McMurdie HF, Evans EH, et al (1981) Nat. Bur. Stand. (U.S.), Monogr. Washington, p 37
59. Smirnov MA, Sokolova MP, Bobrova NV et al (2018) Synergistic effect of chitin nanofibers and polyacrylamide on electrochemical performance of their ternary composite with polypyrrole. J Energy Chem 27:843–853. https://doi.org/10.1016/j.jechem.2017.06.002
60. Arjomandi J, Lee JY, Ahmadi F et al (2017) Spectroelectrochemistry and electrosynthesis of polypyrrole supercapacitor electrodes based on gamma aluminum oxide and gamma iron (III) oxide nanocomposites. Electrochim Acta 251:212–222. https://doi.org/10.1016/j.electacta.2017.08.141
61. Moyseowicz A, Śliwak A, Miniach E, Gryglewicz G (2017) Polypyrrole/iron oxide/reduced graphene oxide ternary composite as a binderless electrode material with high cyclic stability for supercapacitors. Compos Part B Eng 109:23–29. https://doi.org/10.1016/j.compositesb.2016.10.036
62. Karaca E, Gökcen D, Pekmez NÖ, Pekmez K (2019) Electrochemical synthesis of PPy composites with nanostructured MnOx, CoOx, NiOx, and FeOx in acetonitrile for supercapacitor applications. Electrochim Acta 305:502–513. https://doi.org/10.1016/j.electacta.2019.03.060
63. Xu C, Puente-Santiago AR, Rodríguez-Padrón D et al (2019) Controllable Design of Polypyrrole-Iron Oxide Nanocoral Architectures for Supercapacitors with Ultrahigh Cycling Stability. ACS Appl Energy Mater 2:2161–2168. https://doi.org/10.1021/acsaem.8b02167
64. Yang Z, Qiu A, Ma J, Chen M (2018) Conducting α-Fe2O3 nanorod/polyaniline/CNT gel framework for high performance anodes towards supercapacitors. Compos Sci Technol 156:231–237. https://doi.org/10.1016/j.compscitech.2018.01.012
65. Wang H, Xu Z, Yi H et al (2014) One-step preparation of single-crystalline Fe2O3 particles/graphene composite hydrogels as high performance anode materials for supercapacitors. Nano Energy 7:86–96. https://doi.org/10.1016/j.nanoen.2014.04.009